



# Effect of Small-Scale Topographical Variations and Fetch from Roughness Elements on the Stable Boundary Layer Turbulence Statistics

Sudheer R. Bhimireddy<sup>1</sup> · Jielun Sun<sup>2</sup> · Junming Wang<sup>1</sup> · David A. R. Kristovich<sup>1</sup> · April L. Hiscox<sup>3</sup>

© The Author(s) 2023

## Abstract

Understanding the influence of roughness and terrain slope on stable boundary layer turbulence is challenging. This is investigated using observations collected from October to November of 2018 during the Stable Atmospheric Variability ANd Transport (SAVANT) field campaign conducted in a shallow sloping Midwestern field. We analyze the turbulence velocity scale and its variation with the mean wind speed using observations up to 10–20 m on four meteorological towers located along a shallow gully. The roughness length for momentum over this complex terrain varied with wind direction from 0.0049 m to a maximum of 0.12 m for winds coming through deciduous trees present in the field. The variation of the turbulence velocity with wind speed shows a transition from a weak wind regime to a stronger wind regime, as reported by past studies. This transition is not observed for winds coming from the tree area, where turbulence is enhanced even for weak wind speeds. For weak stratification and stronger winds, the turbulent velocity scale increased with an increase in roughness while the terrain slope is seen to have a weak influence. The sizes of the dominant turbulent eddies seen from the vertical velocity power spectra are observed to be larger for winds coming through the tree area. The turbulence enhancement by the trees is found to be strong within a fetch distance of 7 times the tree height and not observable at 16 times of the tree height.

**Keywords** HOckey-stick transition (HOST) · Micro-topography · Shallow gully · Stable boundary layer turbulence · Surface roughness

---

✉ Sudheer R. Bhimireddy  
sudheer@illinois.edu

<sup>1</sup> Climate and Atmospheric Science Section, Division of State Water Survey, Prairie Research Institute, University of Illinois, Champaign, IL, USA

<sup>2</sup> NorthWest Research Associates, Boulder, CO, USA

<sup>3</sup> Department of Geography, University of South Carolina, Columbia, SC, USA

## 1 Introduction

In the atmosphere, a stably stratified boundary layer (SBL) forms most often due to the radiative cooling process after sunset or when warm air is advected above a relatively cold surface (Mahrt 2014). Understanding the onset and physical processes of the SBL has been the subject of various observational studies in the past. The SBL structure is sensitive to processes such as turbulent mixing, radiative cooling, gravity waves, and the interaction with the land surface. The complexity in representing the SBL accurately using the numerical models comes from the nonlinear interactions between the physical processes mentioned before (Holtslag 2006; LeMone et al. 2019). Many models rely on parameterizations for representing the turbulent fluxes as a function of the stability and local conditions. With the increase in computational resources, the spatial and temporal scales at which these models can run has reduced to sub-kilometer scale (LeMone et al. 2019; Bou-Zeid et al. 2020) and thus the small-scale heterogeneities (e.g., topography, aerodynamic roughness, terrain slope, surface temperature) have become significant in deciding the model accuracy.

Most of our current understanding about the SBL is from field campaigns having extensive observations collected over a long period of time (multiple nights or months). Some well-known and well-documented campaigns having quality turbulence measurements at multiple heights within the SBL are (1) the Cooperative Atmosphere–Surface Exchange Study (CASES99, Poulos et al. 2002) conducted in Kansas during October of 1999 over relatively flat terrain with many nights having clear skies, (2) Surface Heat Budget of the Arctic Ocean experiment (SHEBA, Andreas et al. 1999) conducted in Arctic region for about 11 months from October of 1997, (3) Shallow Cold Pool experiment (SCP, Mahrt et al. 2014) conducted in Colorado during October–December of 2012 over shallow topography, (4) the Boundary-Layer Late Afternoon and Sunset Turbulence field campaign (BLLAST, Lothon et al. 2014) conducted in France during June–July of 2011 over complex and heterogeneous terrain, and recently the Stable Atmospheric Variability AND Transport field campaign (SAVANT, Hiscox et al. 2023) conducted in central Illinois during September–November of 2018 over a shallow slope terrain with isolated roughness elements (trees, grasses, corn and soybean crops before harvest and stubbles after harvest). Together, data from such campaigns helped us in categorizing the SBL as either a weakly-stable boundary layer (wSBL) having moderate to strong winds, cloudy conditions and/or weak surface cooling or a very stable boundary layer (vSBL) with weak winds, clear sky conditions and/or strong surface cooling (Mahrt 2014). While such broad classification and our current understanding of the underlying physical processes work well for relatively flat or simple terrain, very few studies focused on the effects of small-scale heterogeneities on the SBL turbulence.

For SBL, turbulence and its relationship with wind speed were commonly parameterized using Monin–Obukhov Similarity Theory (MOST, Monin and Obukhov 1954). MOST based relations were one of the widely used and accepted for characterizing the physical process in the SBL. However, many studies have shown that MOST based similarity relations do not represent the observations well for various SBL conditions over relatively homogeneous terrain (Grachev et al. 2013; Sun et al. 2020) and complex terrain (Nadeau et al. 2013; Babić et al. 2016). Using data from CASES99, Sun et al. (2012, 2016) studied the SBL turbulence variables (e.g., friction velocity, square root of turbulence kinetic energy, vertical velocity variance) and found a threshold wind speed ( $V_s$ ) at a given local and height that can differentiate the weak turbulence regime (having strongly stable conditions) from the strong turbulence regime (weakly stable or near-neutral conditions). Additionally, the transition from weak to strong turbulence during SBL observed by Sun et al. (2012) led to the HOckey-Stick

Transition (HOST) hypothesis. According to HOST, the turbulence mixing in the surface layer at the observation height is due to the most-energetic, turbulent eddies with finite size that are caused by bulk shear between the observation height and the surface rather than the local shear as considered in MOST. The HOST hypothesis has been confirmed/observed at sites having different conditions (e.g., van de Wiel et al. 2012; Bonin et al. 2015; Mahrt et al. 2015; Yus-Diez et al. 2019; Acevedo et al. 2021). External factors controlling the SBL turbulence and its transition between regimes (i.e.,  $V_s$ ), especially close to the surface, could be the terrain features in complex topographical locations (Yus-Diez et al. 2019, Acevedo et al. 2021), or surface roughness (Mahrt et al. 2013), or roughness elements like canopy layer/crops (Dias-Júnior et al. 2017; Bhimireddy et al. 2022; Vendrame et al. 2023), or a combination of the above mentioned (Babic et al. 2016).

The present study uses SBL observations collected during the SAVANT field campaign (Hiscox et al. 2023) to investigate the effect of upstream tall trees, fetch distance from the trees, and terrain slope on the variation of turbulence with wind speed. This paper is organized as follows: Sect. 2 details the topography characteristics and instrumentation used during SAVANT. Section 3 presents the observed turbulence variables and their variations as function of wind speed and direction as well as the discussion of impacts of the tree roughness, terrain slope, and the tree fetch distance on the SBL turbulence characteristics. Section 4 presents the summary of the analysis presented.

## 2 Observations and Methodology

### 2.1 Site Characteristics

The SAVANT field campaign was conducted near Mahomet, Illinois, during September–November 2018. The campaign was conducted in an agricultural field with a shallow-slope topography, one main gully and two feeder gullies. Field schematics along with gullies identified are given in Fig. 1. The main gully (MG) is 1040 m long and 8.9 m wide at the narrowest point, with an elevation difference of 10.7 m between the top and bottom. The feeder gullies FG1 and FG2 are 592, and 226 m long and 15, and 8 m wide respectively. The elevation difference across FG1 and FG2 are 4.9 and 4.6 m respectively. The gully itself was filled with 25–30 cm tall grass. Another feeder gully FG3 connects to the main gully at its end. By October 16, 2018, all the crop in the field was harvested and observations collected after this date (post-harvest) are used in this study.

The wind direction sectors chosen at each tower in Fig. 1 have different upwind conditions (more details in Sect. 3.2). To the southeast of lconv tower, a sparse line of deciduous trees of heights between 20 and 26 m is present, and to the south of lconv tower, multirow deciduous shrubs and two rows of deciduous trees of average height 28 m are present. These are considered as the windbreaks in the present study. To the southwest of rel and uconv towers, and southeast of init tower the terrain slope varies significantly.

### 2.2 Instrumentation and Data Processing

Data for the present study were collected on four Integrated Surface Flux System (ISFS) towers from NCAR Earth Observing Laboratory (EOL) Lower Atmospheric Observing Facilities. Tower locations are shown in Fig. 1. Out of the four towers, two were 10 m tall and others were 20 m tall. The 10 m tall towers were named Initiation (init) tower, and Upper-convergence

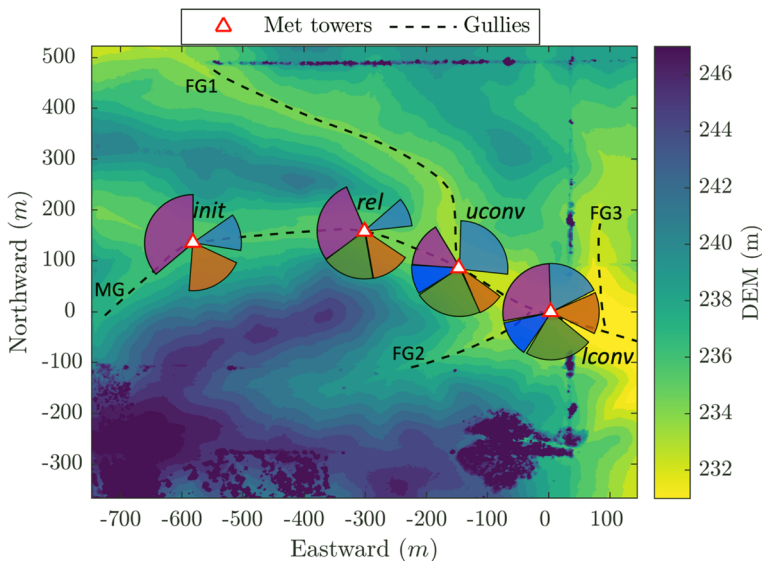


**Fig. 1** SAVANT field Digital Elevation Model (DEM) contour map with gullies represented as dashed lines and ISFS towers shown as white triangles. The italic labels are the respective tower names. The terrain elevation is shown in the color bar. Locations with rapid increases in height as compared to surrounding points indicate trees. Wind direction sectors considered in this study for each tower are drawn as filled sectors. The axis distance is with respect to the lconv tower location, i.e., 40.2103 N, 88.4037 W, positive x-values represent Eastward distance and positive y-values represent Northward distance

(uconv) tower, and the 20 m tall towers were named the Release (rel) tower, and the Lower-convergence (lconv) tower. Data were collected from 15 September to 27 November 2018. Campbell Scientific CSAT3A sonic anemometers were used to measure 3D wind components at a 20 Hz rate. These were located at 1.5, 3, 4.5, 6, and 10 m above surface on all towers, and additional CSAT3A anemometers were located at 8.5, 15, and 20 m on the rel and lconv towers (Hiscox et al. 2023). Sensiron SHT75 humidity and temperature sensors were used to get the 20 Hz observations at 0.2, 1.5, 4.5, and 10 m on all towers, and additionally at 8.5, 15 and 20 m on rel and lconv towers. The Corn and Soybean crop were harvested by 16 October 2018 and the present study uses data collected from these ISFS towers from night of 17 October 2018 to 27 November 2018. Data used in this study are available to download from the EOL website (<https://doi.org/10.26023/NKWR-EYWS-5J0W>).

The initial quality control of the data and the tilt corrections for sonic anemometers deployed during SAVANT were performed by the EOL. Data processing techniques followed to obtain the time averaged variables were described in detail in Bhimireddy et al. (2022), here we provide a brief description. Following Vickers and Mahrt (2003), the multi-resolution flux decomposition (MRFD) of the data identified that a time averaging window of 5 min is sufficient to filter out the influence of mesoscale variations during SAVANT. The SBL observations were chosen as data collected from 1900 central daylight time (CDT = UTC – 5 h) to 0700 CDT of the following day, which matches with the approximate sunset and sunrise times during the campaign. Further, we define the post-harvest nights as nighttime periods starting from 17 October 2018 to 27 November 2018.

## 2.3 Topography and Terrain Slope Estimation

The local terrain slope at each tower was estimated as a function of direction in 1-degree azimuthal angle increments using high-resolution digital elevation model (DEM) data obtained from a Elanus Duo twin-motor fixed wing unmanned aerial system (UAS) flown on April 24, 2019 (Petty 2019). The UAS was flown in an east-west oriented rectangular survey pattern while taking nadir-viewing high-resolution ( $3000 \times 4000$  pixels) images every 1 s from an altitude of 120 m above ground level when there was no crop cover in the field. These images were tagged with the UAS GPS location and were converted to 1-m horizontal resolution DEM data using the commercial Agisoft Metashape software. Centered at each ISFS tower, the DEM points within each azimuthal angle were extracted and the terrain slope was estimated from a linear fit to the DEM points. Terrain slope ( $S\%$ ) from each tower is estimated using the linear fit of the elevation change with radial distance from the tower ( $R$ ). We calculated the terrain slope  $S\%$  for radial distances ranging from 100 to 500 m in 50 m increments. The value of  $S\%$  varied consistently with both direction and radial distance at all the towers with a variability of  $\pm 0.14\%$  for  $R \geq 300$  m up to  $R = 500$  m. Thus, for the remainder of this work, we use the slope values calculated within a 300 m radial distance from each tower.  $S\%$  at 300 m radial distance varied between  $-2\%$  and  $+6\%$  at the SAVANT field site (negative slopes indicate terrain is rising as one approaches the tower). The terrain elevation varied significantly for ‘init’ and ‘rel’ towers along N–S direction as seen in Fig. 1. We did not estimate the surface curvature or assign a single terrain slope value as done in Hurst et al. (2012) or Medeiros and Fitzjarrald (2014) due to the SAVANT field site having large variations in surface elevation within a small area.

## 3 Results and Discussion

### 3.1 Post-harvest SBL Characteristics During SAVANT

The mean profiles of wind speed, turbulent kinetic energy, and potential temperature gradient during post-harvest nights of the SAVANT campaign were discussed in Bhimireddy et al. (2022). Here, we provide the distribution of static stability as measured by the potential temperature difference ( $\Delta\bar{\theta}$ ) taken between the observation height and 0.2 m level. Figure 2 shows the frequency distribution of 5-min averaged  $\Delta\bar{\theta}$  and 10-m wind speed  $\bar{U}_{10\text{m}}$  for post-harvest nights. A total of 5,670 5-min averaged points were used for each observation height on each tower during post-harvest nights. The percentage of 5-min  $\Delta\bar{\theta}$  less than 1 K is 63.4% for the init tower, 67.7% for the rel tower, 67.4% for the uconv tower, and 55.8% for the lconv tower, respectively. The percentage of 5-min wind speeds stronger than  $3 \text{ m s}^{-1}$  for the four towers is 47% (init), 49.8% (rel), 46% (uconv), and 34.5% (lconv), respectively. The time periods with  $\Delta\bar{\theta} < 1 \text{ K}$  over the surface layer of 10 m were classified as neutral or near neutral; these often occurred when the 5-min averaged  $\bar{U}_{10\text{m}}$  at the 10 m observation height was larger than  $3 \text{ m s}^{-1}$  at all the towers except at the lconv tower. One of the objectives of SAVANT field campaign is to collect observations of drainage flows. The procedure for detecting drainage flow during SAVANT was given in Bhimireddy et al. (2022). Here we concentrate on the SBL turbulent mixing in response to terrain slope changes when no drainage flows were detected, for that, 5-min time periods with detected drainage flow were removed from further analysis.

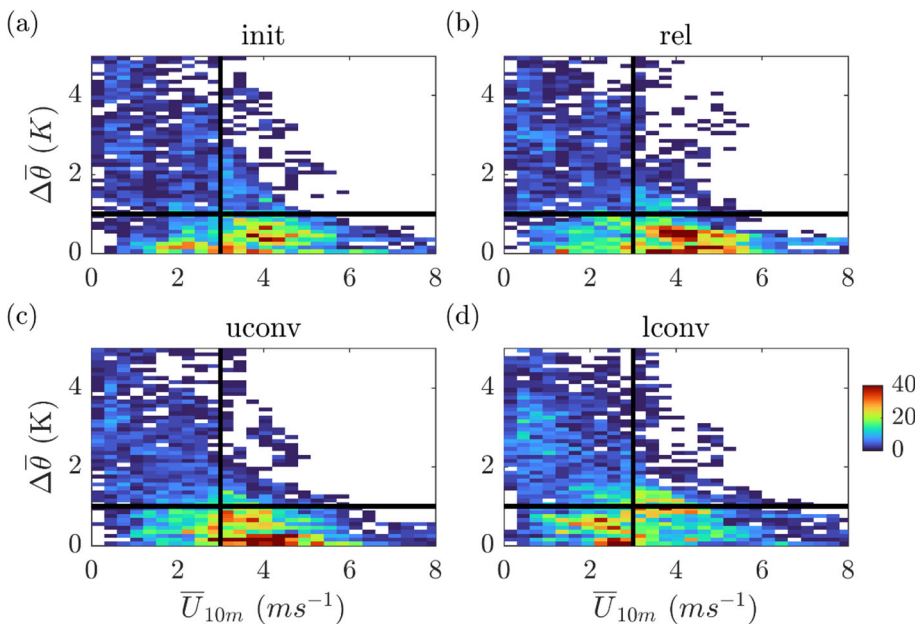


**Fig. 2** 2-D Histogram of bulk  $\Delta\bar{\theta}$  variation with wind speed at 10 m height on **a** init, **b** rel, **c** uconv, and **d** lconv towers. The bulk  $\Delta\bar{\theta}$  is calculated between 10 m and 0.2 m heights. Wind speed bins are  $0.3 \text{ m s}^{-1}$  wide and  $\Delta\bar{\theta}$  bins are  $0.1 \text{ K}$  wide. The colorbar represents the number of 5-min data points falling in each of the bins. The thick horizontal and vertical lines in each subplot represents  $\Delta\bar{\theta} = 1 \text{ K}$  and wind speed =  $3 \text{ m s}^{-1}$  respectively

### 3.2 Impacts of Roughness and Terrain Slope on Turbulent Mixing in SBL

Following Sun et al. (2012), the turbulent velocity scale ( $V_{TKE}$ ) defined as  $V_{TKE} = [0.5(\sigma_u^2 + \sigma_v^2 + \sigma_w^2)]^{1/2}$  where  $\sigma$  represents the standard deviation of the velocity components, was calculated for each observation height at the towers. Variation of post-harvest nighttime  $V_{TKE}$  with wind speed at 1.5 m observation height on each tower is given in Fig. 3. The data were bin-averaged into wind speed bins of  $0.3 \text{ m s}^{-1}$  width. The  $V_{TKE}$  variation in each wind speed bin represented by the vertical bar in Fig. 3, increases with increasing wind speed; this feature is consistent with the observations from CASES99 (Sun et al. 2012, 2020). The increase in the standard deviation of  $V_{TKE}$  at higher wind speeds is due to a reduced number of observations compared to the other wind speed bins. Using the bin-averaged values, a threshold wind speed is defined below which the  $V_{TKE}$  variation with wind speed is negligibly small (Sun et al. 2012). For winds stronger than the threshold wind ( $V_s$ ), the  $V_{TKE}$  starts increasing linearly with wind speed. From Fig. 3, this threshold wind speed is estimated to be  $1.05 \text{ m s}^{-1}$  for init and rel towers, and  $0.45 \text{ m s}^{-1}$  for uconv tower. For lconv tower, the bin-averaged  $V_{TKE}$  values increased with wind speed even for weak winds and no threshold wind speed is identifiable. Once the wind speed increases beyond the threshold wind speed, the  $V_{TKE}$  values increase with wind speed at a constant rate of  $\sim 0.24$  at init, rel and uconv towers, mixing the air between the observation height and the surface level. This indicates that the dominant turbulent eddies are generated by bulk shear as demonstrated in Sun et al. (2016, 2020). The less dramatic change between the weak and strong wind regimes

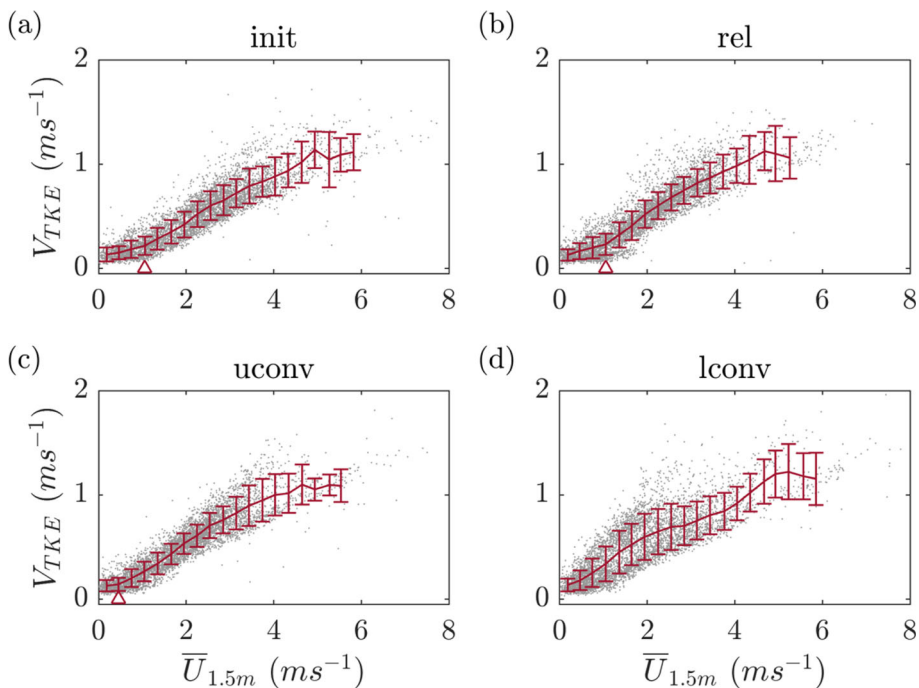


**Fig. 3** Variation of 5-min averaged  $V_{TKE}$  variation with wind speed at 1.5 m observation height on (a) init, (b) rel, (c) uconv and (d) lconv towers. The vertical lines represent the standard deviation

here in comparison with the one found by Sun et al. (2012) could be influence of clouds during SAVANT on the  $V_{TKE}$ - $\bar{U}$  relationship as discussed in Sun et al. (2020).

To further understand the different  $V_{TKE}$ - $\bar{U}$  trends, we examined the variation of  $V_{TKE}$  normalized by wind speed at a given observation height with wind direction as shown in the left column of Fig. 4. This ratio between  $V_{TKE}$  and mean wind speed could be considered turbulence intensity (TI) at a given height and Fig. 4 shows that it is sensitive to the wind direction. For winds coming from West and generally aligned with the main gully, a significant number of time periods had a weak TI magnitude and strong static stability. A significant increase in the TI values ( $TI > 0.3$ ) can be noted for winds coming from SE-SW near the lconv tower. Winds from E (i.e., up-gully direction) at the lconv tower were generally moderate with wind speed values larger than  $2 \text{ m s}^{-1}$  and had higher  $V_{TKE}/\bar{U}$  values. The static stability as measured by  $\partial\bar{\theta}/\partial z$  between 10 and 0.2 m observations heights was higher for winds aligned with main gully. Overall, two conclusions can be drawn based on Figs. 1 and 4) the magnitude of TI for similar stability and wind speed was much higher at lconv tower compared to the other sites for the wind directions between 130 and 200 deg, and 2) the magnitude of stability and TI varied with wind direction at all the towers.

To further investigate the dependence of TI on wind direction at the lconv tower, we calculated wind speed and  $V_{TKE}$  at the lconv tower relative to the uconv tower at the 1.5 m observation level as shown in Fig. 5. For wind directions between 135 and 200 deg, we found that the 30-min averaged wind speeds are usually weaker at lconv than uconv while the  $V_{TKE}$  magnitudes are generally stronger at lconv than uconv (Fig. 5). Figure 1 indicates that the air flow from this wind direction sector to lconv is strongly influenced by trees. This

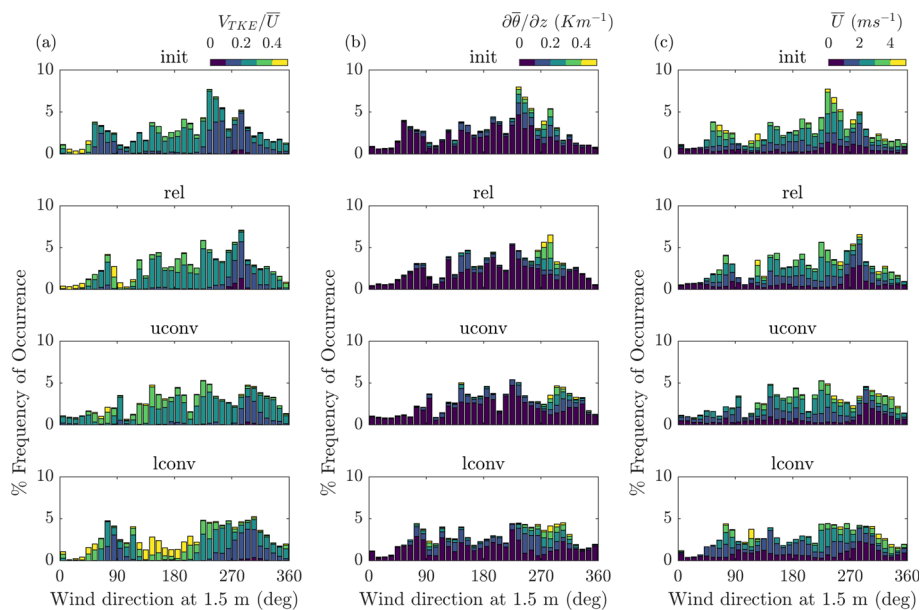


**Fig. 4** Percentage frequency of occurrence of **a**  $V_{TKE}/\bar{U}$  at 1.5 m observation height, **b** static stability measured as the difference between potential temperatures between 10 m and 0.2 m observation heights, and **c**  $\bar{U}$  at 1.5 m observation height with wind direction at 1.5 m observation level at each tower for post-harvest nights during SAVANT

observed turbulence enhancement with relatively weak velocity was not observed for other wind directions at the lconv tower. In the absence of such additional roughness elements, one would expect similar wind speed and turbulence magnitudes between the lconv and uconv towers as the horizontal distance between them is only 158 m. For wind directions between 65 and 115 deg, we see that the 30-min wind speeds are stronger at lconv than uconv while the  $V_{TKE}$  magnitudes are weaker at lconv than uconv. This wind direction represents winds traveling up-gully at the lconv tower. For different wind direction sectors than discussed above, similar dependence of velocity and  $V_{TKE}$  deficits with wind direction were observed at other towers (not shown). The opposite behavior of velocity and  $V_{TKE}$  deficits for 135–200 deg and 65–115 deg wind directions at the lconv tower highlight the roughness and terrain slope influence on local conditions.

To distinguish impacts of roughness and terrain slope on turbulent mixing, we investigate variations of roughness with the within-300-m terrain slope at all the towers. Because  $V_{TKE}$  is closely related to the friction velocity,  $u_*$  (e.g., Sun et al. 2012), an increase of  $V_{TKE}$  with wind speed, that is, the slope of  $V_{TKE}$  versus  $\bar{U}$ , would be related to drag coefficient defined as  $C_d = (u_*/\bar{U})^2$ . For the strong turbulence regime under nearly neutral conditions (i.e.,  $\bar{U} > V_s$ ), the  $V_{TKE}$ - $\bar{U}$  slope would be directly related to roughness, which is indeed confirmed by Mahrt et al. (2013). We, therefore, concentrate on the strong turbulence regime with winds greater than  $V_s$  and examine the  $V_{TKE}$ - $\bar{U}$  slope as a function of wind direction. To ensure statistically meaningful results, we select wind-direction sectors with the minimum number of 300 5-min average data points in each wind direction sector. As a result, three sectors for the init tower, four for the rel tower, and five sectors for both uconv and lconv towers are selected (Table 1).

Using the criteria,  $|\bar{\theta}_{10m} - \bar{\theta}_{0.2m}| < 1K$  and  $\bar{U}_{10m} > 3m s^{-1}$ , i.e., near-neutral conditions, the roughness length for momentum ( $z_0$ ) was estimated based on the methodology of Sun (1999). We give the summary of this method here. For detailed description see Sun (1999). Based on MOST and using bulk-formula, for near-neutral conditions considered here,  $z_0$  is related to the mean wind speed through  $\ln(z/z_0) = \bar{U}(z)\kappa/u_*$ , where  $\kappa (= 0.41)$  is the von Kármán constant. The roughness length for momentum at each tower is obtained using the 30-min time averaged wind speed and momentum flux observations at multiple levels.  $z_0$  values listed as a function of wind direction at each tower are given in Table 1. Overall, the largest shift in roughness length with wind direction was observed at the lconv tower with  $z_0$  value of 0.0049 m for wind directions in the range of 67 and 114 degrees (up gully flow), and a  $z_0$  value of 0.1205 m for wind directions in the range of 133 to 204 degrees (dense trees located to the south of the lconv tower).

The variation of  $V_{TKE}$  with wind speed in Fig. 3 is redrawn for the selected wind sectors at each tower (Fig. 6). At the init tower, for the winds coming from 100 to 181 degrees (down-slope winds),  $V_{TKE}$  starts increasing linearly with wind speed for  $\bar{U} > 0.8 m s^{-1}$  making it the threshold wind speed ( $V_s$ ) required to reach near-neutral stability for that wind direction. For the wind directions 57–98 and 226–360 degrees, the  $V_{TKE}$  increase with wind speed starts at  $\bar{U} > 1.5 m s^{-1}$  at a different rate. The  $V_{TKE}$ - $\bar{U}$  slope varied a lot at the lconv tower, from 0.23 for 67–114 deg wind directions (up-gully) to 0.435 for 133–204 deg wind directions (from trees). The  $V_{TKE}$ - $\bar{U}$  slope for down-gully directions is 0.23 for init, rel, and uconv towers, and 0.224 at lconv tower. For comparison, the  $V_{TKE}$ - $\bar{U}$  slope estimated from CASES99 dataset was 0.25 (Sun et al. 2012).

Different  $V_{TKE}$ - $\bar{U}$  slope and the  $V_s$  values for winds coming from sloped (mountainous) terrain compared to winds coming over relatively flat terrain is previously reported using observations from the BLLAST field campaign (Yus-Diez et al. 2019). The terrain conditions present at SAVANT site are different from CASES99 (relatively flat) and BLLAST campaigns

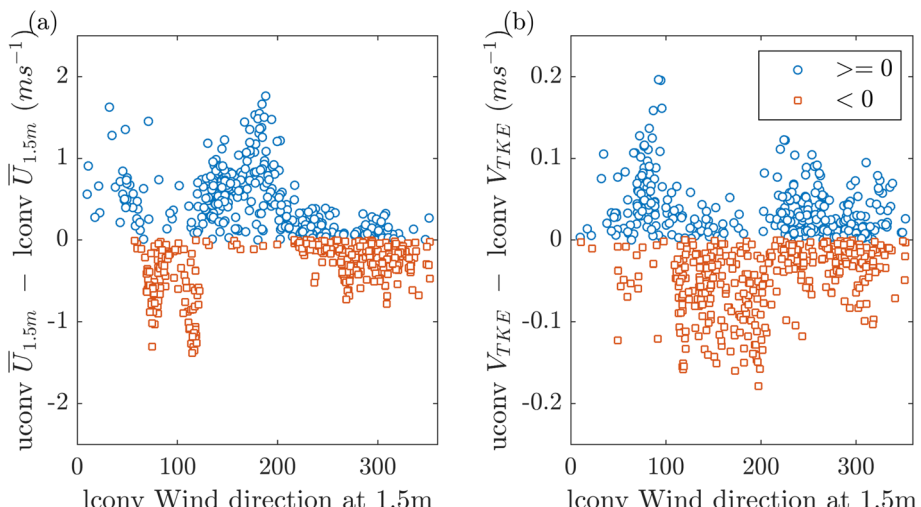


**Fig. 5** Variation of 30 min average **a** velocity difference, and **b** difference in the  $V_{TKE}$  magnitude between 1.5 m observation height on uconv and lconv towers, plotted against the wind direction observed at 1.5 m on lconv tower. Positive values are colored blue, while negative values are colored red

(complex topography), which gives us a unique opportunity to study the feedback of such gentle terrain differences on the stable boundary layer turbulence.

To understand the feedback of the terrain on the turbulent mixing at SAVANT site, we calculated the correlation coefficient between the vertical velocity and potential temperature,  $-R_{w\theta}$  (defined as  $\overline{w'T'}/\sigma_w\sigma_T$ , and gives the efficiency of turbulence mixing) and  $\Delta\bar{\theta}$  (between the observation height and 0.2 m level). Figure 7 shows the variation of  $V_{TKE}$ ,  $-R_{w\theta}$  and  $\Delta\bar{\theta}$  at init and lconv towers for along gully wind directions. At 1.5 m observation height on init tower, for down-gully directions,  $-R_{w\theta}$  value increased with wind speed from 0.2 and reached a maximum value of 0.4 at  $\bar{U} = 2 \text{ m s}^{-1}$  and decreased thereafter with increase in wind speed. Meanwhile,  $\Delta\bar{\theta}$  between 1.5 m and 0.2 m levels decreased gradually from 1 K to 0.6 K for  $\bar{U}$  values increased from 0  $\text{m s}^{-1}$  to 2  $\text{m s}^{-1}$  and decreased rapidly with further increasing wind speed, while the  $V_{TKE}$  value remained low for  $\bar{U} \leq 2 \text{ m s}^{-1}$  and increased linearly for  $\bar{U} > 2 \text{ m s}^{-1}$  making  $V_s = 2 \text{ m s}^{-1}$  at  $z = 1.5 \text{ m}$  on init tower for down-gully winds. Similar variation of  $-R_{w\theta}$ ,  $\Delta\bar{\theta}$  and  $V_{TKE}$  was observed for other heights on init tower and at lconv tower. With an increase in observation height, the value of  $V_s$  increased suggesting that stronger winds are required to initiate the vertical mixing (Sun et al. 2012, 2016).

Next, we study the  $V_{TKE}$ ,  $-R_{w\theta}$  and  $\Delta\bar{\theta}$  variation with wind speed for up-gully wind direction sectors at init and lconv towers and present the results for 1.5 and 10 m observation levels in Fig. 8, along with the data for 1.5 and 10 m levels from Fig. 7. At init tower 1.5 m level, similar to down-gully winds, the  $V_{TKE}$  increased linearly with wind speed starting for  $\bar{U} > 2 \text{ m s}^{-1}$  while  $-R_{w\theta}$  reached a maximum value of about 0.39 just before  $\bar{U} = 2 \text{ m s}^{-1}$ .

**Table 1** List of roughness lengths for momentum ( $z_0$ ) and average terrain slope (S%) with in 300 m radius from the tower location for each tower during SAVANT post-harvest time periods

Tower name	Wind direction range (deg)	$z_0$ (m)	Average terrain slope (S%) in 300 m radius	Terrain feature
init	57–98	0.0138	0.58	Up-gully
	100–181	0.0239	3.26	Down-slope
	226–360	0.0219	0.87	Down-gully
rel	50–79	0.0260	0.83	Up-slope
	127–170	0.0262	1.34	Up-slope
	170–231	0.0659	4.12	Down-slope
	235–340	0.0555	1.84	Down-gully
uconv	3–97	0.0350	1.57	Down-slope
	131–156	0.0214	0.65	Up-slope
	156–232	0.0421	3.17	Down-slope
	239–276	0.0532	4.49	Down-slope
	276–330	0.0292	2.02	Down-gully
lconv	0–60	0.0915	2.21	Trees
	67–114	0.0049	–0.59	Up-gully
	133–204	0.1205	2.34	Trees
	212–254	0.0669	3.18	Down-slope
	259–360	0.0317	2.08	Down-gully

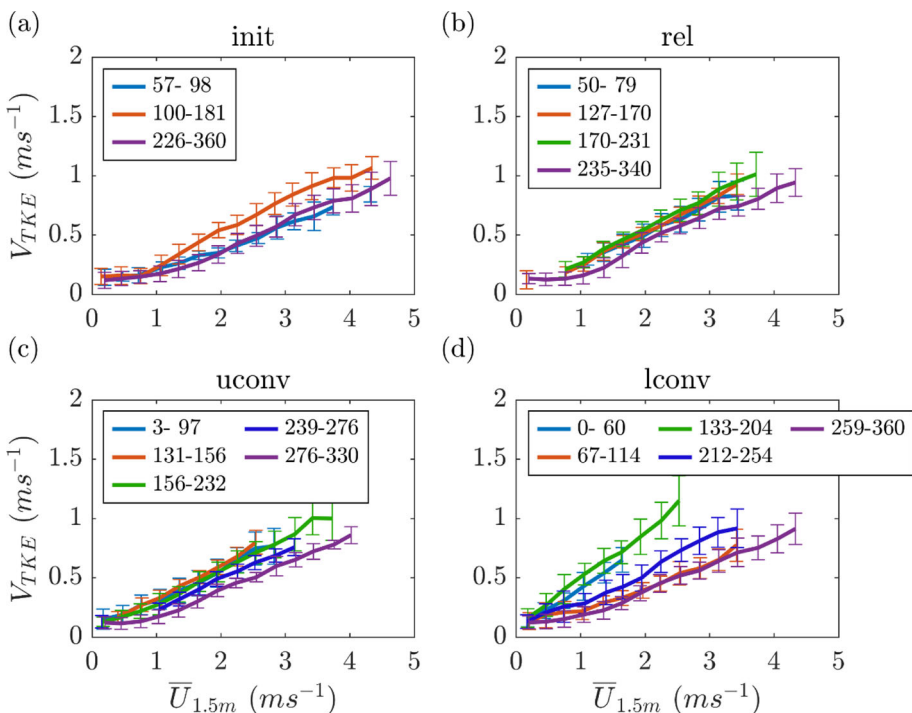


**Fig. 6** Same as Fig. 3, but bin-averaged and data at each tower is divided into wind directions listed in Table 1. The thin vertical lines represent the standard deviation. Only bins with more than 20 observations were considered for averaging. Colors used in the figure represent individual tower wind direction sectors as shown in Fig. 1

For  $\bar{U} < 1 \text{ m s}^{-1}$ ,  $\Delta\bar{\theta}$  observed at all levels on init tower for up-gully winds is barely higher than those seen for down-gully winds. Similar behavior of  $V_{TKE}$  with  $\bar{U}$  was observed at lconv tower for up-gully winds. At lconv tower,  $-R_{w\theta}$  values for  $\bar{U} < 2 \text{ m s}^{-1}$  were lower than the init tower values. Smaller  $-R_{w\theta}$  values at lconv tower suggests weaker mixing, which should be associated with a stronger stratification, but the  $\Delta\bar{\theta}$  values observed were similar to at the init tower, which is unexpected. Using observations from Shallow Cold Pool (SCP) campaign, Mahrt (2022, 2022) recently reported similar trends where larger  $\Delta\bar{\theta}$  values occurred when  $-R_{w\theta}$  was higher and vice versa for towers located on top and bottom of a sloped terrain.

To investigate the structure of coherent eddies for different wind directions, we analyzed the normalized vertical velocity spectra,  $fS_w/\sigma_w^2$ , where  $f$  is frequency,  $S_w$  is the power spectrum of vertical velocity, and  $\sigma_w$  is the standard deviation of vertical velocity, at all observation levels on the uconv tower. Sun et al. (2012, 2016, 2020) found that the size of large coherent eddies responsible for mixing was close to the observation height during neutral conditions (or during  $\bar{U} > V_s$ ) and that the size scale of dominant turbulent eddies decreases with increasing atmospheric stability. To investigate the effect of terrain features and avoid the influence of the atmospheric stratification on  $V_{TKE}$ , we select three different time periods of 4-h windows when wind speed is stronger than the threshold wind speed and wind directions with different dominant terrain influences (i.e., down-slope, down-gully, tree area) as shown in Fig. 9. Looking at Fig. 9, during each period considered, the normalized

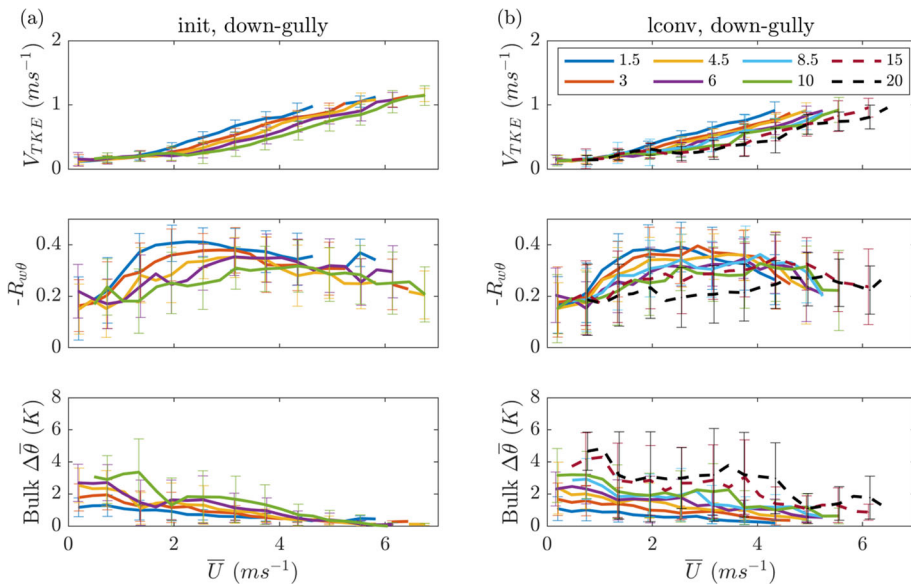


**Fig. 7** Variation of  $V_{TKE}$ ,  $-R_{w\theta}$ , and  $\Delta\bar{\theta}$  on **a** init, and **b** lconv towers at the observation heights for down-gully wind directions. The thin vertical lines represent the standard deviation. Only bins with more than 20 5-min averaged observations were considered for averaging

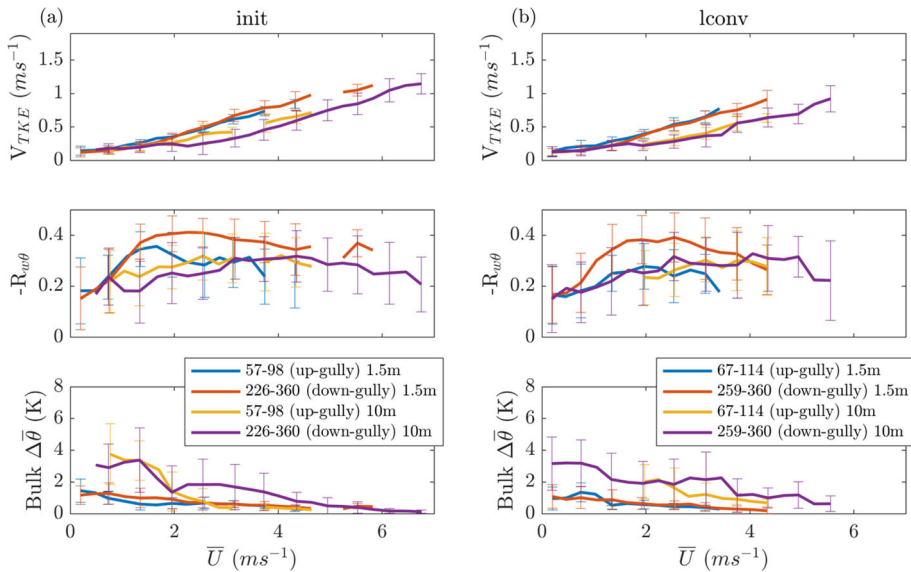


**Fig. 8** Variation of  $V_{TKE}$ ,  $-R_{w\theta}$ , and  $\Delta\bar{\theta}$  on **a** init, and **b** lconv towers for up-gully wind direction compared with the down-gully wind direction mentioned in the subplot legends. The thin vertical lines represent the standard deviation. Only bins with more than 20 observations were considered for averaging

vertical velocity spectra at all the observation levels on uconv reached their peaks at the same normalized frequency value ( $zf/\bar{U}$ ), suggesting that the surface layer is nearly neutral (Sun et al. 2020). Based on the spectral peak, the value of normalized frequency at the maximum  $fS_w/\sigma_w^2$  differed with the wind direction. The normalized spectra reached its peak with  $zf/\bar{U} = 0.3$  for winds through the tree area direction,  $zf/\bar{U} = 0.5$  for winds coming down the main gully, and  $zf/\bar{U} = 0.65$  for winds coming in the down-slope direction. Considering the wind direction shown in Fig. 9a as reference, the normalized spectral peak shifted to higher frequencies for wind flowing down the main gully and wind flowing down the slope. This indicates that the turbulent eddy scales are influenced by the roughness elements and terrain slope and the tree area enhances the scale of the most energetic, turbulent eddies with the maximum normalized turbulence intensity.

Various quantities at the 1.5 m observation level averaged over the time periods shown in Fig. 9 are listed in Table 2. At 1.5 m above the surface when the wind speeds are similar, the downward turbulent heat fluxes for flow along the downslope are around 30% and 178% stronger compared to when the flow is aligned with the main gully and flow coming over the windbreaks respectively. Between the flow aligned with the main gully and the downslope directions, the value of  $-R_{w\theta}$ , turbulent kinetic energy, variance of vertical velocity and horizontal wind speed are stronger for downslope direction. This increase in turbulence and its efficiency in mixing could be due to the microscale variation of turbulent transport in response to the downslope terrain variation. Mahrt (2022) recently found that the turbulence lee of a downslope is altered compared to its upwind value at the SCP site. Since the observations during SAVANT are limited to the main gully, tracking the changes in the turbulent quantities from upwind to downwind of the downslope feature is not possible. Interestingly, between the flow aligned with downslope direction (Fig. 9b) and the flow coming through the windbreaks (Fig. 9a), the turbulent kinetic energy ( $\bar{e}$ ) and variance of horizontal wind speed were stronger for windbreak flow but the downward turbulent heat flux, variance of vertical velocity and  $-R_{w\theta}$  were weaker. The contributions of variances of vertical velocity and horizontal wind speed to the turbulent kinetic energy varied significantly for windbreak flow, where the horizontal fluctuations contribute about 86% of  $\bar{e}$  estimated. This value is about 76% for flow aligned with the main gully.

Overall, the turbulence magnitude and its vertical structure downwind of either the windbreaks or a change in terrain slope is affected. However, more observations are required (especially along the downslope terrain) to understand the modification of the air flow due to the microscale terrain features.

The calculated  $V_{TKE}-\bar{U}$  slope for each wind direction sector considered in this study is plotted against the momentum roughness length in Fig. 10. Overall, the  $V_{TKE}-\bar{U}$  slope increased with increase in  $z_0$ . For the wind direction sectors with trees,  $V_{TKE}-\bar{U}$  slope was significantly higher compared to the rest. Such high  $V_{TKE}-\bar{U}$  slope value indicates enhanced vertical turbulent mixing even for low winds ( $\bar{U} < 2 \text{ m s}^{-1}$ ).

### 3.3 Effect of Fetch Distance on the Downwind Turbulence Structure

To understand how the impact of the tree roughness on  $V_{TKE}$ ,  $-R_{w\theta}$  and  $\Delta\bar{\theta}$  vary with the fetch distance between the roughness element (tree area) and the observation tower location, we studied the variation of  $V_{TKE}$ ,  $-R_{w\theta}$  and  $\Delta\bar{\theta}$  at three levels (1.5, 10 and 20 m) on the rel and lconv towers. For this, only winds coming through the tree area to the individual towers were chosen (highlighted as shaded sectors in Fig. 11a). For this analysis, observations at init tower were excluded because winds coming from this direction are subjected to steep slope

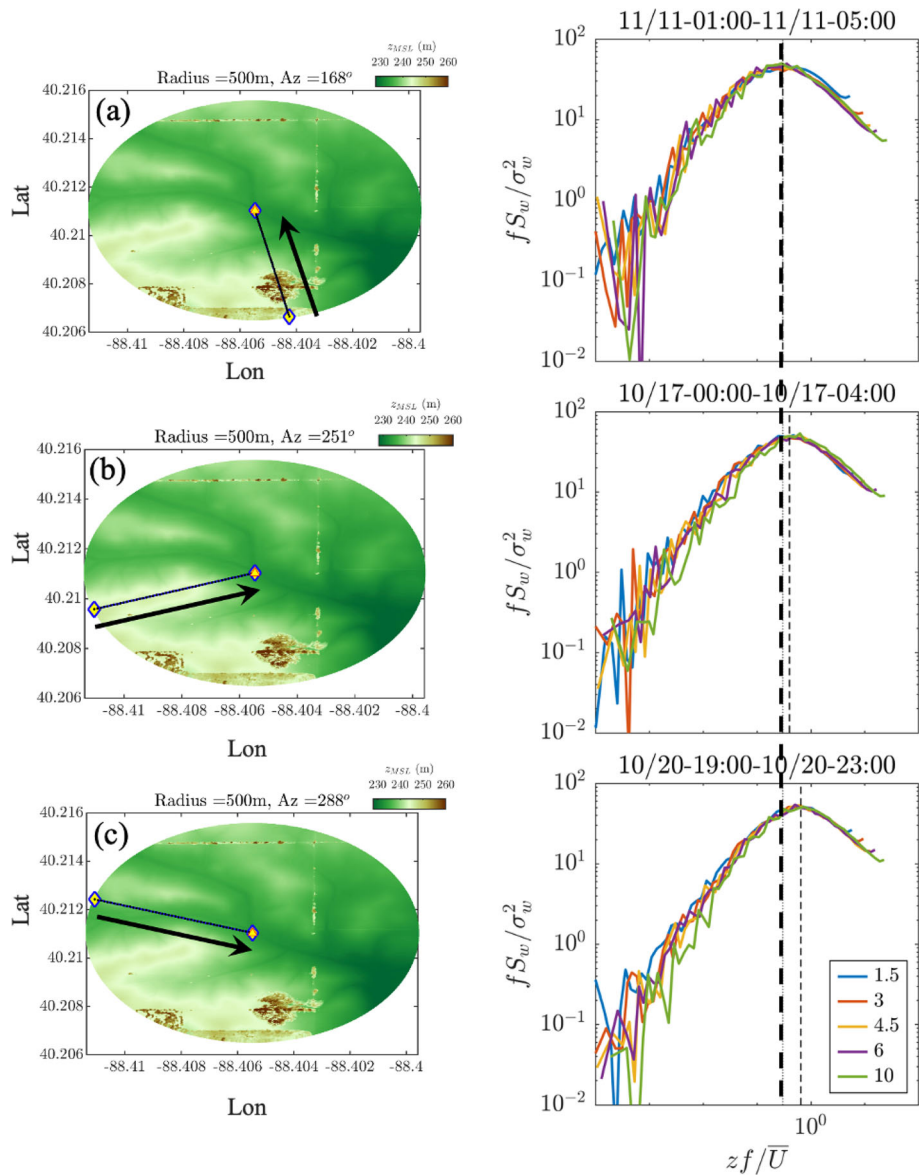
**Table 2** 4-h average values at 1.5 m observation height on the uconv tower for time periods listed in Fig. 9

Variable	11/11-0100-0500 CDT	10/17-0000-0400 CDT	10/20-1900-2300 CDT
$\bar{U} \left( \text{m s}^{-1} \right)$	2.3	2.2	2.35
$\bar{w' \theta'} \left( 10^{-3} \text{ Km s}^{-1} \right)$	- 14	- 39	- 30
$-R_{w\theta}$	0.37	0.44	0.39
$\sigma_w \left( \text{m s}^{-1} \right)$	0.27	0.32	0.24
$\sigma_U \left( \text{m s}^{-1} \right)$	0.87	0.79	0.58
$\bar{e} \left( \text{m}^2 \text{ s}^{-2} \right)$	0.44	0.37	0.22

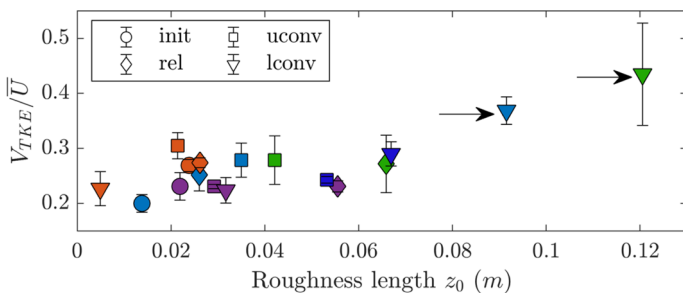
variations due to the hill present in between the tree area and the init tower. Likewise, the observations at uconv tower were also excluded as the highest observation level (i.e., 10 m) is below the tree base. The fetch distance between the tree area and each tower was normalized by the average tree height ( $H=28$  m). Then, the rel tower with an average fetch of 16 H is the farthest observation location from the tree line, while the lconv tower with a fetch of just 7 H is the closest one.

Figure 12 gives the variation of  $V_{TKE}$ ,  $-R_{w\theta}$  and  $\Delta\bar{\theta}$  at three levels (1.5, 10, and 20 m) on the rel and lconv towers for winds coming through the tree area. The  $V_{TKE}$  at lconv tower was higher than that at rel tower irrespective of the wind speed at each of the observation level shown in the figure. The dependence of observational levels can be seen for  $-R_{w\theta}$ , where the difference between the  $-R_{w\theta}$  values increased with height. In line with the  $-R_{w\theta}$  differences observed among the rel and lconv towers, the bulk  $\Delta\bar{\theta}$  with the 0.2 m level was smaller at the lconv tower for 10 and 20 m levels. This suggests that even for weak winds coming through the trees the downwind turbulence transfer of heat or mixing in the vertical was stronger at lconv tower resulting in the lower  $\Delta\bar{\theta}$ . Recently, Mahrt and Acevedo (2022) reported that  $-R_{w\theta}$  values decrease rapidly with height for strongly stable stratification and in the absence of external factors such as wind directional shear or surface heterogeneity. They observed that the  $-R_{w\theta}$  variation with height is more complex (sometimes  $-R_{w\theta}$  stayed constant with height) when a “regional boundary layer” forms aloft due to the upwind rougher surfaces. In comparison with the observed decrease of  $-R_{w\theta}$  with height for up- and down-gully flows (Fig. 8), the observed increase of  $-R_{w\theta}$  at lconv suggests that the roughness due to the trees contributes to the enhanced turbulent mixing through efficient turbulent transfer in the vertical as seen from the increased  $-R_{w\theta}$  values with height. Due to the terrain sloping from tree base to the tower location, observation levels below 10 m are below the tree base at both rel and lconv tower, and the  $-R_{w\theta}$  value remained more or less constant with height at the rel tower, while it remained constant only up to 6 m and later increased with height at the lconv tower (not shown), suggesting a complex vertical layer structure connecting the levels below the tree base with levels above the tree base.

As windbreaks are used quite often in the agricultural fields across the U.S. and other countries, knowing how far from the windbreak does the turbulence intensifies for a given upwind wind speed could help farmers in determining the optimal location for dispersion of pesticides and control the pesticide drift (Ucar et al. 2001). Although the atmospheric response downwind of the windbreak depends on the windbreak properties (such as porosity, shape,



**Fig. 9** (left column) DEM surrounding the uconv tower, and (right column) normalized vertical velocity spectra at all observation levels on uconv tower for **a** flow over tree line direction during 0100–0500 CDT on 11/11/2018, **b** down slope flow during 0000–0400 CDT on 10/17/2018, and **c** down gully flow during 1900–2300 CDT on 10/20/2018. The thick dash line drawn across the panels represents the  $zf/\bar{U}$  value when the  $fS_w/\sigma_w^2$  reached its peak. The thin dash line in the right panels of (b) and (c) represents the  $zf/\bar{U}$  value when the  $fS_w/\sigma_w^2$  reached its peak in **(a)** for comparison



**Fig. 10** Variation of  $V_{TKE}/\bar{U}$  slope with  $z_0$  at each tower and wind direction sector. The wind direction at each tower is represented by the marker color which is same as in Fig. 1. Markers with right-pointing arrows represent wind directions from the tree area. The error bars are drawn based on the scatter present in the estimated  $V_{TKE}/\bar{U}$  slope for each wind direction sector

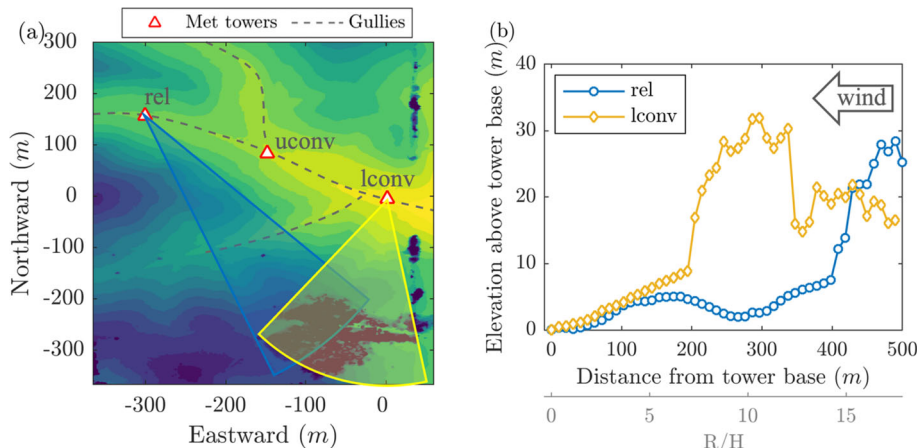


**Fig. 11** **a** DEM near the rel and lconv towers and the tree patch with sectors drawn for winds coming through the tree patch and on to the towers. **b** Variation of elevation relative to the tower base with the radial distance ( $R$ ) from the tower for the sectors identified in (a) for rel and lconv towers. The light-colored x-axes at the bottom of subplot (b) is normalized by the tree height ( $H$ ). The winds are coming on to the towers

internal structure, and arrangement; Wang and Takle 1996; Brandle et al. 2021), findings from the present study are thought to be applicable to similar sites and stability conditions. Future observations with dense network and other variety of windbreaks would improve our understanding of other mechanisms contributing to the enhanced turbulent and mixing in the downwind.

## 4 Summary

The effect of terrain slope, roughness length and fetch from roughness elements (trees) on the stable boundary layer turbulence characteristics were studied using tower observations collected during the SAVANT field campaign. Post-harvest stable boundary layer observations collected up to 10–20 m on four meteorological towers installed along a shallow gully were

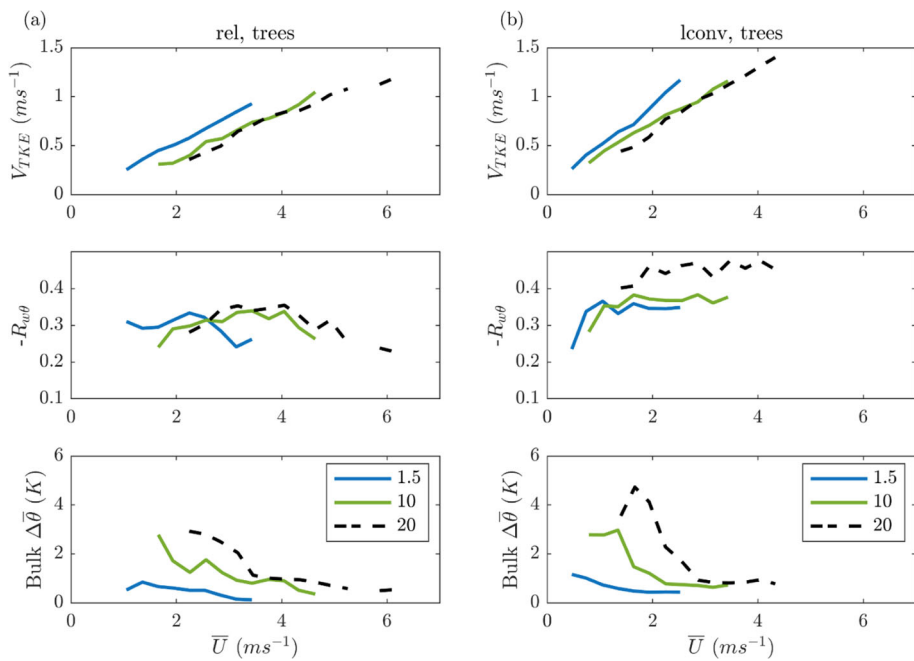


**Fig. 12** Variation of  $V_{TKE}$ ,  $-R_{w\theta}$ , and bulk  $\Delta\bar{\theta}$  at 1.5 m, 10 m, and 20 m heights on (a) rel and (b) lconv towers for wind directions through the trees. Only bins with more than 20 5-min averaged observations were considered

used to evaluate the turbulent velocity scale ( $V_{TKE}$ ), and correlation coefficient between the vertical velocity fluctuations and temperature. The 5-min averaged values of  $V_{TKE}$  normalized by the wind speed, bulk static stability calculated between 10 m and 0.2 m observation heights, and the velocity deficit calculated between the adjacent towers varied significantly with wind direction at each of the four observation towers. The roughness length for momentum at the towers varied from 0.0049 m (bottom of the main gully) to 0.1205 m (for winds coming over the windbreaks). In general, the rate of  $V_{TKE}$  increase with wind speed is seen to increase with roughness length, as found in the past studies. However,  $V_{TKE}$  increased modestly with wind speed when the roughness is due to terrain heterogeneity, and it increased greatly when the roughness is due to the trees.

During near-neutral conditions under strong winds, the scale of the most energetic eddies with the maximum variance value in the vertical velocity spectra is enhanced when the winds are downslope and is further enhanced when the winds are coming through the trees. The added roughness due to the trees resulted in reduction of the mean wind speed, increase in the turbulence and correlation between the temperature and vertical velocity fluctuations at the downwind location. We found that during near-neutral conditions turbulence caused by the bulk shear is strongly influenced by the fetch from roughness elements and weakly influenced by the terrain slope.

A complex vertical layer exists connecting the observations below the tree base with the ones above it. To study the composite effect of trees and terrain slope in detail, high-resolution observations are needed in vertical with levels beyond the tree height. Understanding these micro-topographical effects on the downwind turbulence is important as the tree-line elements present during the SAVANT field campaign were a part of windbreak structures that are common in the agricultural fields present in the Midwest US.

**Acknowledgements** The authors thank UCAR staff and several students who participated in SAVANT and are responsible for generating the dataset. The authors would like to thank the three anonymous reviewers for their valuable feedback on the work presented. Opinions expressed are those of the authors and not necessarily those of the Illinois State Water Survey, the Prairie Research Institute, or the University of Illinois.

**Funding** Funding for this study was provided by NSF AGS Awards 22200662, 22200663 and 22200664.

## Declarations

**Conflict of interest** The authors declare no conflict of interest.

**Open Access** This article is licensed under a Creative Commons Attribution 4.0 International License, which permits use, sharing, adaptation, distribution and reproduction in any medium or format, as long as you give appropriate credit to the original author(s) and the source, provide a link to the Creative Commons licence, and indicate if changes were made. The images or other third party material in this article are included in the article's Creative Commons licence, unless indicated otherwise in a credit line to the material. If material is not included in the article's Creative Commons licence and your intended use is not permitted by statutory regulation or exceeds the permitted use, you will need to obtain permission directly from the copyright holder. To view a copy of this licence, visit <http://creativecommons.org/licenses/by/4.0/>.

## References

Acevedo OC, Costa FD, Maroneze R, Carvalho AD, Puhales FS, Oliveira PE (2021) External controls on the transition between stable boundary-layer turbulence regimes. *Q J R Meteorol Soc* 147(737):2335–2351

Andreas EL, Fairall CW, Guest PS, Persson POG (1999) An overview of the SHEBA atmospheric surface flux program, In: Proceedings of Fifth Conference on Polar Meteorology and Oceanography, Dallas, TX, Amer Meteorol Soc, pp. 550–555

Babić K, Rotach MW, Klaić ZB (2016) Evaluation of local similarity theory in the wintertime nocturnal boundary layer over heterogeneous surface. *AgricFor Meteorol* 228:164–179

Bhimireddy SR, Wang J, Hiscox AL, Kristovich DA (2022) Influence of stability and surface roughness on turbulence during the stable atmospheric variability and transport (SAVANT) field campaign. *J Appl Meteorol Climatol* 61(9):1273–1289

Bonin TA, Blumberg WG, Klein PM, Chilson PB (2015) Thermodynamic and turbulence characteristics of the southern great plains nocturnal boundary layer under differing turbulent regimes. *Boundary-Layer Meteorol* 157:401–420

Bou-Zeid E, Anderson W, Katul GG, Mahrt L (2020) The persistent challenge of surface heterogeneity in boundary-layer meteorology: a review. *Boundary-Layer Meteorol* 177:227–245

Brandle JR, Takle E, Zhou X (2021) Windbreak practices. North American Agroforestry. American Society of Agronomy, Madison, pp 89–126

Dias-Júnior CQ, Sá LD, Marques Filho EP, Santana RA, Mauder M, Manzi AO (2017) Turbulence regimes in the stable boundary layer above and within the Amazon forest. *Agric For Meteorol* 233:122–132

Grachev AA, Andreas EL, Fairall CW, Guest PS, Persson POG (2013) The critical Richardson number and limits of applicability of local similarity theory in the stable boundary layer. *Boundary-Layer Meteorol* 147:51–82

Hiscox A, Bhimireddy S, Wang J, Kristovich DA, Sun J, Patton EG, Oncley SP, Brown WO (2023) Exploring influences of shallow topography in stable boundary layers: the SAVANT Field Campaign. *Bull Am Meteorol Soc* 104(2):520–541

Holtslag AAM (2006) Preface: GEWEX atmospheric boundary-layer study (GABLS) on stable boundary layers. *Boundary-Layer Meteorol* 118(2):243–246

Hurst MD, Mudd SM, Walcott R, Attal M, Yoo K (2012) Using hilltop curvature to derive the spatial distribution of erosion rates. *J Geophys Res Earth Surf* 117:F2

LeMone MA, Angevine WM, Bretherton CS, Chen F, Dudhia J, Fedorovich E, Katsaros KB, Lenschow DH, Mahrt L, Patton EG, Sun J (2019) 100 years of progress in boundary layer meteorology. *Meteorol Monograph* 59:9.1–9.86

Lothon M, Lohou F, Pino D, Couvreux F, Pardyjak ER, Reuder J, Vilà-Guerau de Arellano J, Durand P, Hartogensis O, Legain D, Augustin P (2014) The BLLAST field experiment: boundary-layer late afternoon and sunset turbulence. *Atmos Chem Phys* 14(20):10931–10960

Mahrt L (2014) Stably stratified atmospheric boundary layers. *Annu Rev Fluid Mech* 46:23–45

Mahrt L (2022) Horizontal variations of nocturnal temperature and turbulence over microtopography. *Boundary-Layer Meteorol* 184(3):401–422

Mahrt L, Acevedo O (2022) Types of vertical structure of the nocturnal boundary layer. *Boundary-Layer Meteorol* 187:141–161

Mahrt L, Thomas C, Richardson S, Seaman N, Stauffer D, Zeeman M (2013) Non-stationary generation of weak turbulence for very stable and weak-wind conditions. *Boundary-Layer Meteorol* 147:179–199

Mahrt L, Sun J, Oncley SP, Horst TW (2014) Transient cold air drainage down a shallow valley. *J Atmos Sci* 71(7):2534–2544

Mahrt L, Sun J, Stauffer D (2015) Dependence of turbulent velocities on wind speed and stratification. *Boundary-Layer Meteorol* 155:55–71

Medeiros LE, Fitzjarrald DR (2014) Stable boundary layer in complex terrain. Part I: linking fluxes and intermittency to an average stability index. *J Appl Meteorol Climatol* 53(9):2196–2215

Monin AS, Obukhov AM (1954) Osnovnye Zakonomernosti turbulentnogo peremeshivaniya v prizemnom sloe atmosfery (Basic laws of turbulent mixing in the atmosphere near the ground). *Trudy Geofiz Inst AN SSSR* 24(151):163–187

Nadeau DF, Pardyjak ER, Higgins CW, Parlange MB (2013) Similarity scaling over a steep alpine slope. *Boundary-Layer Meteorol* 147(3):401–419

Petty G (2019) SAVANT Field Site Orthophoto and High-Resolution DEM. Version 1.0. UCAR/NCAR-Earth Observing Laboratory. <https://doi.org/10.26023/9X98-348Q-V14>

Poulos GS, Blumen W, Fritts DC, Lundquist JK, Sun J, Burns SP, Nappo C, Banta R, Newsom R, Cuxart J, Terradellas E (2002) CASES-99: a comprehensive investigation of the stable nocturnal boundary layer. *Bull Am Meteorol Soc* 83(4):555–582

Sun J (1999) Diurnal variations of thermal roughness height over a grassland. *Boundary-Layer Meteorol* 92:407–427

Sun J, Mahrt L, Banta RM, Pichugina YL (2012) Turbulence regimes and turbulence intermittency in the stable boundary layer during CASES-99. *J Atmos Sci* 69(1):338–351

Sun J, Lenschow DH, LeMone MA, Mahrt L (2016) The role of large-coherent-eddy transport in the atmospheric surface layer based on CASES-99 observations. *Boundary-Layer Meteorol* 160:83–111

Sun J, Takle ES, Acevedo OC (2020) Understanding physical processes represented by the Monin–Obukhov bulk formula for momentum transfer. *Boundary-Layer Meteorol* 177(1):69–95

Ucar T, Hall FR (2001) Windbreaks as a pesticide drift mitigation strategy: a review. *Pest Manag Sci Former Pestic Sci* 57(8):663–675

van de Wiel BJH, Moene AF, Jonker HJJ, Baas P, Basu S, Donda JMM, Sun J, Holtlag AAM (2012) The minimum wind speed for sustainable turbulence in the nocturnal boundary layer. *J Atmos Sci* 69(11):3116–3127

Vendrame N, Tezza L, Pitacco A (2023) Evolution of turbulent flow characteristics in a hedgerow vineyard during the growing season. *Agric For Meteorol* 328:109251

Vickers D, Mahrt L (2003) The cospectral gap and turbulent flux calculations. *J Atmos Oceanic Technol* 20:660–672

Wang H, Takle ES (1996) On three-dimensionality of shelterbelt structure and its influence on shelter effects. *Boundary-Layer Meteorol* 79:83–105

Yus-Díez J, Udina M, Soler MR, Lothon M, Nilsson E, Bech J, Sun J (2019) Nocturnal boundary layer turbulence regimes analysis during the BLLAST campaign. *Atmos Chem Phys* 19(14):9495–9514